JOURNAL OF SPACECRAFT AND ROCKETS
Vol. 41, No. 3, May–June 2004

Direct Simulation Monte Carlo Method on Rarefied Hypersonic Flow Around Flat Plates

Nobuyuki Tsuboi*
Institute of Space and Astronautical Science, Kanagawa 229-8510, Japan
and
Hiroki Yamaguchi† and Yoichiro Matsumoto‡
University of Tokyo, Tokyo 113-8656, Japan

The flow over a sharp flat plate with a finite leading-edge angle located in a rarefied hypersonic flow was investigated numerically with the direct simulation Monte Carlo method using the dynamic molecular collision model based on the molecular dynamics simulation of nitrogen molecules. The results of the two-dimensional numerical simulations of the zero-leading-edge-angle plate did not agree with the experimental results in the middle cross section of the span direction. Thus, to investigate much more precisely about the detailed physical phenomena in the rarefied hypersonic flow over the sharp flat plate, three-dimensional numerical simulations were performed. At first, to compare with the two-dimensional simulation, the leading-edge effects and the finite span effects were investigated. From these numerical simulations, the flowfield around the plate was shown to be three-dimensional, and the effects were evaluated to determine the three-dimensional flow structure over the plate. Finally, the nonequilibrium flow over the plate showed that non-Maxwell–Boltzmann distributions for translational and rotational energy distributions are clearly apparent.

Nomenclature

C_H	=	local heat transfer coefficient
E_{rot}	=	rotational energy, J
E_{rot_0}	=	rotational energy at ground state, J
E_{tr}	=	translational energy, J
Kn	=	Knudsen number
L	=	reference length, m
M_∞	=	freestream Mach number
p_0	=	stagnation pressure, Pa
p_∞	=	freestream pressure, Pa
R	=	gas constant, J/(kg · K)
Re	=	Reynolds number
T_{rot}	=	rotational temperature, K
T_{tr}	=	translational temperature, K
T_w	=	wall temperature, K
T_0	=	stagnation temperature, K
T_∞	=	freestream temperature, K
t_{ref}	=	reference time step, s
$\bar{V}$	=	rarefaction parameter
V_∞	=	freestream velocity, m/s
X, Y, Z	=	x, y, z coordinates, m
λ_∞	=	mean free path in freestream, m
ρ_∞	=	freestream density, kg/m^3

Introduction

MANY researchers have been studying hypersonic rarefied gas flows around space vehicles with respect to viscous interaction. Viscous interaction is defined as a mutual interaction between external flowfield and boundary-layer growth around a body of given shape. In particular, hypersonic viscous interaction near a leading edge in a rarefied regime shows significant interaction between shock wave and boundary-layer growth and includes strong nonequilibrium between molecular internal degrees of freedom. A schematic of viscous interaction near a leading edge is shown in Fig. 1. For the continuum flow regime, strong and weak interaction is governed near the leading edge. However, a merged layer, where it is difficult to distinguish between the shock wave and the boundary layer, develops near the leading edge for rarefaction parameter $\bar{V} > 0.15$ (Ref. 1). The three-dimensional nonequilibrium merged layer has not been discussed in detail because there are few experiments for three-dimensional merged-layer nonequilibrium flows.

For numerical simulations of hypersonic flows in the rarefied regime, the direct simulation Monte Carlo (DSMC) method[2,3] is valid, whereas the continuum approach may be inappropriate. Lengrand et al.[4–7] conducted DSMC simulations and experiments in a rarefied gas flow around a flat plate, and they explained the existence of nonequilibrium between translational and rotational temperature by using DSMC simulations. The DSMC results agreed qualitatively with the experimental results for wall pressure and heat transfer rate; however, the Larsen–Borgnakke (LB) model[8] was applied for the gas–gas collision, which gave only a fair estimate of the nonequilibrium phenomena. Multiscale models have recently been developed using the molecular dynamics (MD) simulation to include information about the microscale phenomena. Tokumasu and Matsumoto have constructed a dynamic molecular collision (DMC) model[9] for nitrogen molecules that is able to predict the nonequilibrium accurately in rarefied gas flow at temperature below 2000 K. The purpose of the present research is to examine both two- and three-dimensional simulations of hypersonic rarefied gas flow over a flat plate using the DSMC method with the DMC model and to reveal the structure of the merged layer.

Numerical Method

DSMC Method

The DSMC method is a powerful technique for the numerical simulations of hypersonic flows in the rarefied regime, whereas the continuum approach may produce inaccurate results for such flow. The gas–gas molecular-collision model plays a significant role in the accuracy of the simulation. Larsen and Borgnakke constructed a gas–gas collision model (LB model)[8] based on the equilibrium

Presented as Paper 2001-1851 at the AIAA/NAL-NASDA-ISAS 10th International Space Planes and Hypersonic Systems and Technologies Conference, Kyoto, Japan, 24–27 April 2001; received 30 October 2001; revision received 6 March 2003; accepted for publication 14 May 2003.

*Associate Professor, High Speed Aerodynamics, Research Division for Space Transportation. Member AIAA.
†Graduate Student, Department of Mechanical Engineering.
‡Professor, Department of Mechanical Engineering. Member AIAA.

property of the molecular energy distributions. Although the LB model has been widely used, the lack of microscale phenomena such as the translational–rotational energy exchange process has given the model some disadvantages.

Recently, multiscale models have been developed based on the MD simulation for a higher reproducibility of the microscale phenomena. The basic concept of the multiscale model is described in Fig. 2. For example, a bow shock wave around a reentry vehicle occurs in a nonequilibrium rarefied flow. In the shock wave, a very large number of molecular collisions occurs between diatomic molecules with energy exchange between the translational and rotational degree of freedom. If we focus on one of the molecular collisions, interactions between atomic nuclei and electrons appear. Such interactions can be simulated by using the Shrödinger equation, but the complicated procedure can be skipped if a molecular potential, such as the Lennard–Jones potential, is used. Using the Lennard–Jones potential, MD simulations of binary collisions with various energies can be performed to obtain the probability density function (PDF) of translational and rotational energy exchange before and after the molecular collisions. Finally, a gas–gas collision model can be constructed that then can be implemented in the DSMC technique to estimate aerodynamic characteristics around the reentry vehicle.

Tokumasu and Matsumoto constructed the DMC model[9] for nitrogen molecules that is able to capture the nonequilibrium characteristics in the rarefied gas flow below 2000 K. The current DMC model is based on the cross sections and energy distributions after the collisions obtained by MD simulations for diatomic molecules. The present DSMC code uses the DMC model for gas–gas collisions, the diffuse reflection for gas–surface interactions, and the null collision technique[10] for collision frequency.

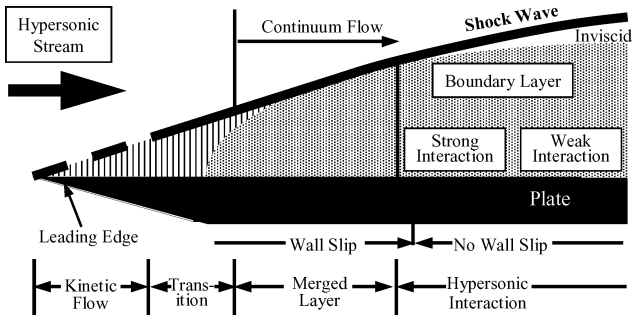

Fig. 1 Schematic of viscous interaction near a sharp leading edge.

Parallel Implementation

To reduce CPU time per processor for three-dimensional simulation, the parallel implementation of the computational code is highly desirable. In the present research, we adopted the domain decomposition method by allocating a subdomain to each processor element (PE) where the calculations are performed for the allocated particles.[11,12] When the particles cross a subdomain boundary, data such as the position, velocity, and energy components are communicated to the appropriate PEs (see Fig. 3).

A problem with parallel DSMC simulations is potentially the large imbalance that can occur for both CPU time and number of particles in each PE. This imbalance problem arises because particle distributions between initial and final simulation states are quite different. To avoid this problem, an active load-balancing method for the allocated subdomain was applied during the parallel simulation by controlling the number of particles in each subdomain.

The data that each PE requires are particle velocity, position, and rotational energy. After the number of particles that cross the subdomain boundary is checked, the information is stored in a temporal array. The reason for this process is that the number of communication subroutines has to be reduced because those subroutines need CPU time before starting to communicate data. Then the data in the temporal array, such as velocity, position, and rotational energy, are communicated to the other PEs. Those data received from the other PEs are stored in the actual arrays.

There are two kinds of existing parallel languages: one is constructed for a special compiler to add some compiler indicator statements in an existed language; another is a parallel language

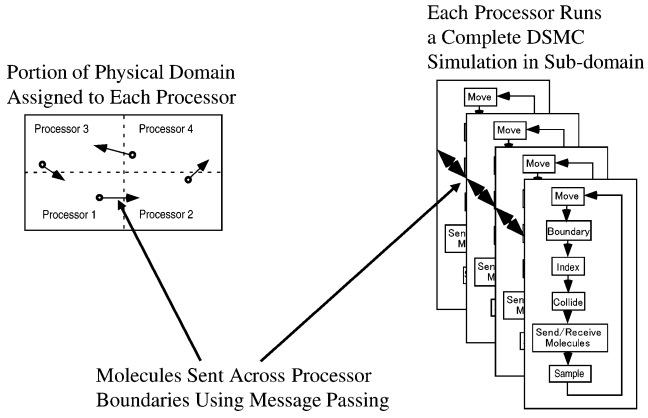

Fig. 3 Schematic of the parallel DSMC method.

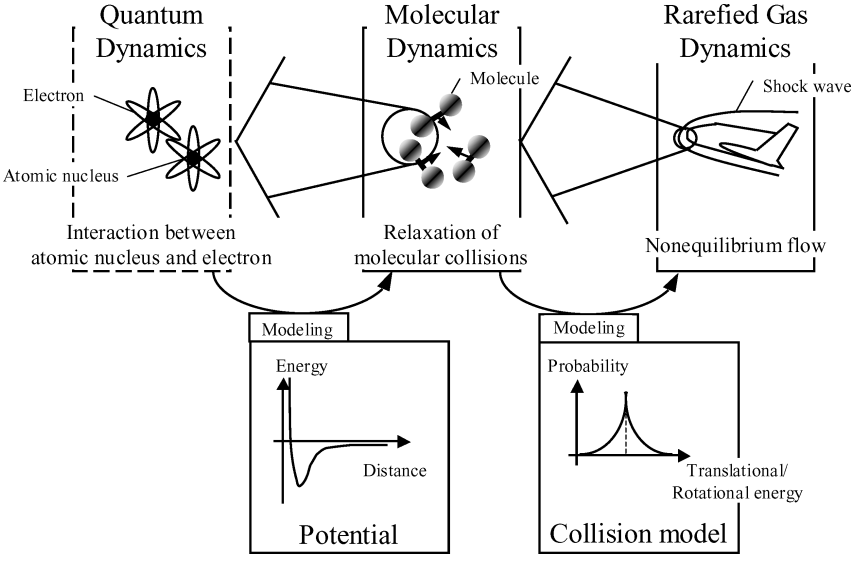

Fig. 2 Schematic diagram of the present multiscale analysis model.

library to enable the parallel processes of the message-passing library (MPL). The former is mainly used as a special parallel language library for a specific special parallel computer. The latter can be used for many parallel computers because the language is an MPL. The parallel virtual machine (PVM) and the message passing interface (MPI) belong to the MPL. Because MPI is one of the common libraries for parallel computing and is not dependent on the parallel computer architecture, MPI was used to parallelize the present DSMC code.

In the aforementioned communication between PEs, point-to-point nonblocking communication routines were used. If the point-to-point blocking communication routines are used, waiting status appears and much communication time is incurred until a send buffer is able to send or a receive buffer receives all data.

The sending process occurs at the specified PE, but the PE has to receive data from other PEs so that a matrix communication is carried out for all PEs. The simulations are synchronized between the movement and the collision routines at each time step.

Results and Discussion

Simulation conditions are shown in Tables 1 and 2. The inflow conditions are those for the experiment conducted by Lengrand et al.[4] In the simulations, the plate has a leading-edge angle of 20 deg. For the dimensions, the plate length is 100 mm, the plate width is 100 mm, and the plate thickness is 5 mm. At the trailing edge, the rarefaction parameter $\bar{V} = 0.55$; consequently, the flowfield over the plate for the present simulation conditions would be in the merged layer or more rarefied regimes. For the uncertainty in the referred experiment, density, pressure, and heat transfer are roughly 10, 15, and 10%, respectively. The reason for the larger uncertainty for pressure is that the difference between pressure in the transducer and the normal force exerted on the plate has a significant effect. These uncertainties include not only those of the measurement system for density, pressure, and heat transfer rate, but also those of the flow conditions.

Figure 4 shows the computational grid systems for the two-dimensional simulation (with finite leading edge, no. 2) and for the three-dimensional simulation (no. 3). The number of computational cells is 3040 for the two-dimensional simulation and 110,493 for the three-dimensional simulation.

Table 1 Computational conditions in the present simulations[a]

No.	Simulation	Leading-edge angle, deg
1	Two dimensional	——
2	Two dimensional	20
3	Three dimensional	20

[a] $M_\infty = 20.2$, working gas is N_2, $p_0 = 3.5 \times 10^5$ Pa, $T_0 = 1100$ K, $T_\infty = 13.32$ K, $p_\infty = 0.06831$ Pa, $V_\infty = 1503$ m/s, $Re_\infty = 566$ (based on $L = 0.05$ m, $2L$ = plate length), $T_w = 290$ K, $Kn_\infty = 0.047$ (based on L), and wall boundary condition is diffuse.

Table 2 Computational conditions for sensitivity analysis and the case for the LB model[a]

No.	Leading-edge angle, deg	Grid[b]	Time step	Number of particles (millions)	Fraction of inerastic collision
1	——	N	0.01	6	——
4	——	C	0.01	6	——
5	——	F	0.01	6	——
6	——	N	0.0005	6	——
7	——	N	0.02	6	——
8	——	N	0.01	3	——
9	——	N	0.01	12	——
10	20	——	0.01	——	$\phi = 0$
11	20	——	0.01	——	$\phi = 0.5$
12	20	——	0.01	——	$\phi = 1$

[a] Other simulation conditions are the same as for Table 1.
[b] N, normal; C, coarse; F, fine.

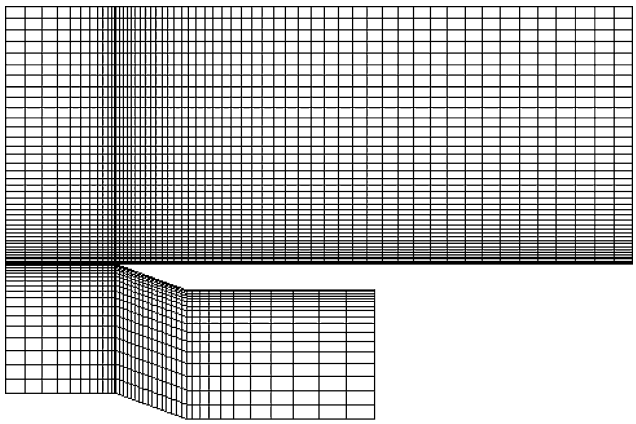

a)

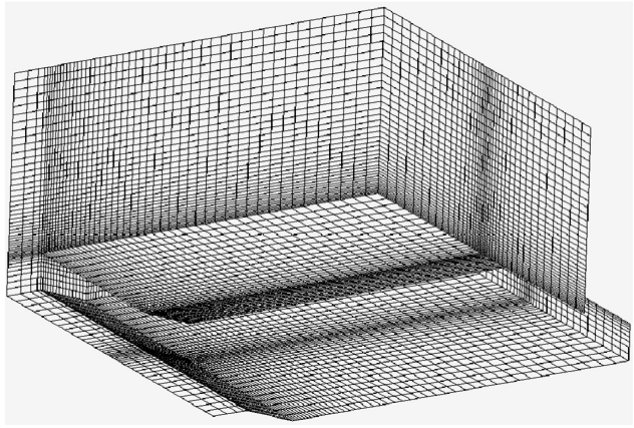

b)

Fig. 4 Computational grid for a) two- and b) three-dimensional simulations.

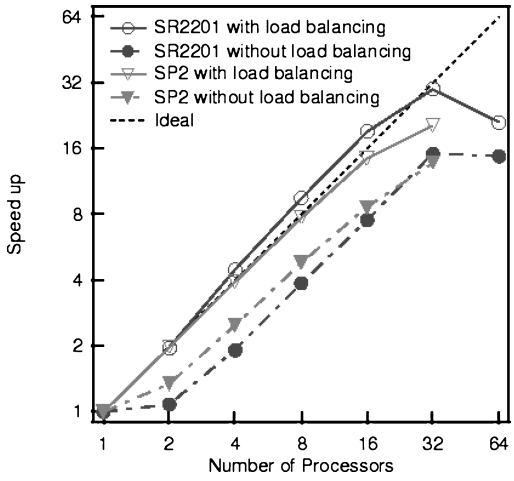

Fig. 5 Speedup for the two-dimensional code (simulation condition 1).

Parallel Performance

The parallel computing performance of the two-dimensional DSMC code was measured for no. 1 (Table 1), on both the IBM SP2 and the Hitachi SR2201. Peak performances for each processor are 266.4 Mflops for the SP2 and 300 Mflops for the SR2201. Interprocessor data payload communication rates are 40 MB/s for SP2 and 266 MB/s for SR2201. The CPU measurement for each case was conducted for a fixed number of time steps, after steady state was reached, and did not include the initialization or I/O costs. Figure 5 shows the results of the speedup of the DSMC code with and without dynamic load balancing. The maximum speedup without dynamic load balancing is 15.13 on the SR2201 (32 PEs) and

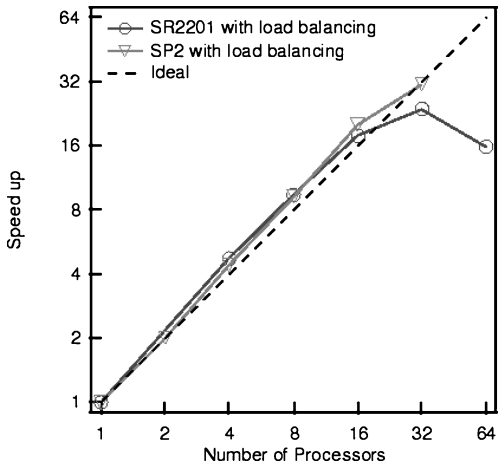

Fig. 6 Speedup for the three-dimensional code (simulation condition 3).

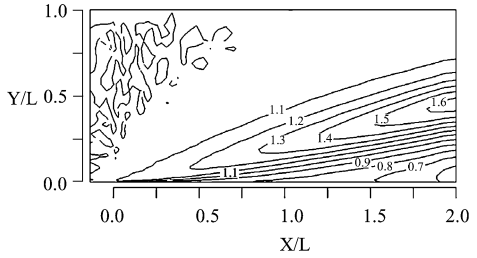

a) Without leading edge (condition 1)

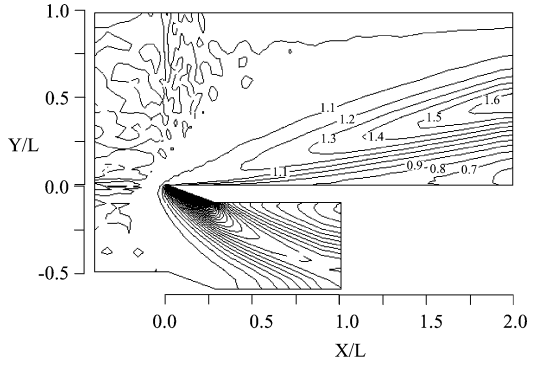

b) With leading edge 20 deg (condition 2)

Fig. 7 Density contours around the plate for the two-dimensional simulation.

13.78 on the SP2 (32 PEs). With dynamic load balancing, the maximum speedup is 30.0 on the SR2201 (32 PEs) and 20.32 on the SP2 (32 PEs). As shown in Fig. 5, the idealized speedup is attained for all combinations of considered processors except for 64 processors.

Figure 6 shows the parallel speedup in the three-dimensional simulations. Almost all cases in the three-dimensional simulations have ideal speedup. From this result, this DSMC parallel computing code with load balancing shows outstanding performance and does not depend on the system or architectures of the machine.

Two-Dimensional Simulation Results

Figure 7 shows density contours around the plate. A thick shock wave is generated near the leading edge in both cases. However, the case LE = 20 (leading edge angle of 20 deg) has a small influence on the contours near the leading edge. Figure 8 shows the effects of the leading edge on density profiles at $X/L = 1.5$. The maximum density location for LE = 20 is farther from the plate surface than that for LE = 0, and the maximum density for LE = 20 is larger than that for LE = 0. However, the DSMC results are slightly different from the experimental results with regard to the maximum density and its location.

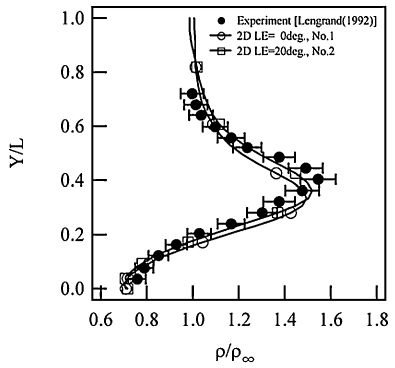

Fig. 8 Effects of plate leading edge on density profiles at $X/L = 1.5$.

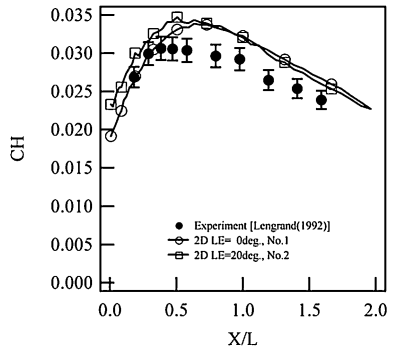

Fig. 9 Effects of plate leading edge on heat transfer rate distributions.

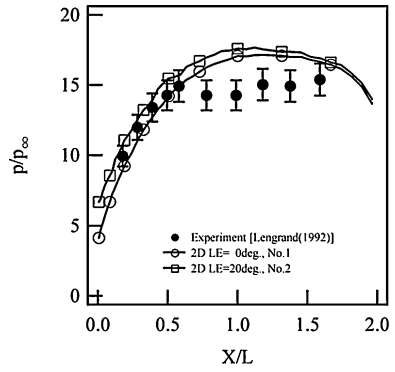

Fig. 10 Effects of plate leading edge on pressure distributions.

Figure 9 shows heat transfer distributions on the plate. Results for LE = 20 shift toward the leading edge and the maximum value for LE = 20 is more than that for LE = 0. The DSMC results are about 16% larger than the experimental results.

Figure 10 shows pressure distributions on the plate. Pressure on the wall in the DSMC simulations is calculated not by macroscopic pressure p derived from the equation of state, which uses density and temperature, but by the total normal momentum exchange of molecules on the wall, F_n. Because the assumption of continuum flow is not valid for the present test case, the pressure at the wall, p, calculated with the ideal gas equation of state does not provide an accurate result. In practice, it is shown[4] that the summation of the normal components of momentum exchange, F_n, agrees well with the experimental results, whereas the pressure calculated by the ideal gas equation of state, p, is too large. Figure 10 shows that the calculated pressure along the wall for LE = 20 increases more than that for LE = 0. DSMC results agree well with the experimental results at $X/L < 0.6$; however, DSMC results overestimate at $X/L > 0.6$. Experimental results have discontinuous distributions, which suggests some possible problems with the experiments.

Figure 11 shows translational and rotational temperature distributions on the plate. These temperatures were calculated in the

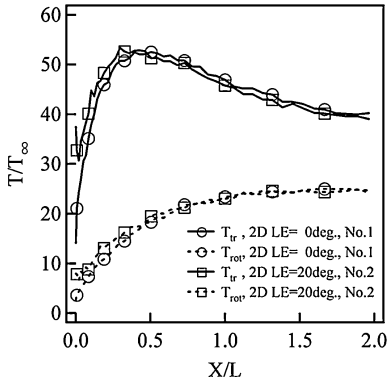

Fig. 11 Effects of plate leading edge on translational and rotational temperature distributions.

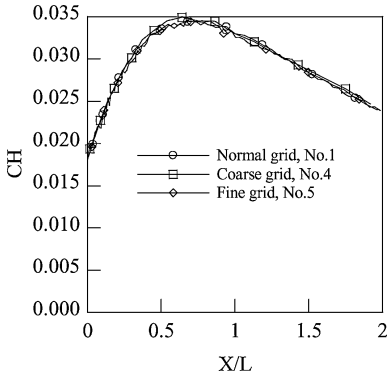

Fig. 12 Effects of the number of grid points on heat transfer rate distributions on the plate.

cell adjacent to the wall. The results indicate that a large nonequilibrium exists between translational and rotational temperatures. Translational and rotational temperature distributions for LE = 20 increase and move toward the leading edge compared with those for LE = 0. The translational temperature distribution for LE = 20 has a sudden increment in the vicinity of the leading edge ($X/L \sim 0$) due to the influence of the strong shock wave below the plate.

Sensitivity Analysis in Two-Dimensional Simulations

Sensitivity analyses in the present simulation are evaluated. Simulation conditions are listed in Table 2. Parameters for the sensitivity analysis are the number of computational cells, time step, and the number of particles. All other conditions are shown in Table 1. The number of computational cells are 2000 for normal grid, 500 for coarse grid, and 8000 for fine grid, respectively. Time step is normalized by $t_{\text{ref}} = \lambda_\infty/\sqrt{(2RT_\infty)}$. The numbers of particles in Table 2 are approximate values.

Figures 12 and 13 show the effect of the number of computational cells on heat transfer rate and temperature distributions on the plate. For the heat transfer rate, this effect does not appear; however, for the temperature distributions, the number of cells clearly affects the translational temperature. Because temperatures are calculated in the cell adjacent to the wall, it is thought that the number of cells easily influences the results. However, the present normal grid is thought to be adequate when compared with the results of the fine grid.

Figures 14 and 15 show the effect of the time step and the number of particles. In the present simulation, there is no influence on the heat transfer rate. Although temperature distributions on the plate are not shown here, results indicate that neither parameter affects the temperature distributions.

Three-Dimensional Simulation Results

Density distributions from a three-dimensional numerical simulation with LE = 20 are shown in Fig. 16. From the results, features of the shock wave are identified along with the size of the leading edge and finite span influence. The finite span effects appear at $Z/L > 0.5$ for $X/L = 1.5$. The finite span effects are caused by three-dimensional viscous effects near the plate side tip. Comparisons between two- and three-dimensional results are shown in Figs. 17 and 18. It is shown that there are small discrepancies between two- and three-dimensional simulations because finite span effects are primary near the span edge, as shown in Fig. 16. It is concluded that the three-dimensional effects are negligible near the symmetry plane and that the flow in this plane can be treated as a two-dimensional flow. Figures 19 and 20 show the normalized translational and rotational temperature contours on the plate. Both temperatures are normalized by the freestream temperature of 13.32 K, and the normalized wall temperature is equal to 21.77 K. Translational temperature increases rapidly near the leading edge, whereas rotational temperature gradually increases. Large nonequilibrium is evident on the whole domain of the plate. Near

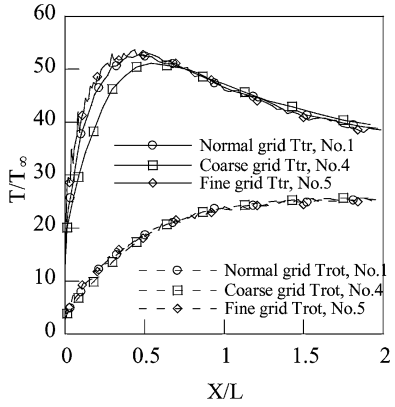

Fig. 13 Effects of the number of grid points on translational and rotational temperature distributions on the plate.

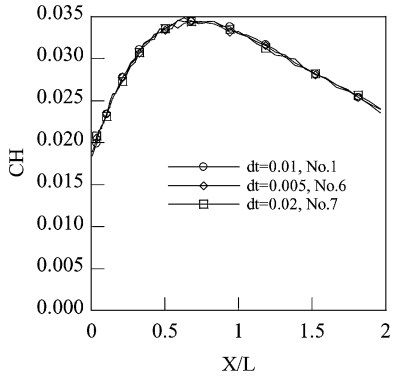

Fig. 14 Effects of time step on heat transfer rate distributions on the plate.

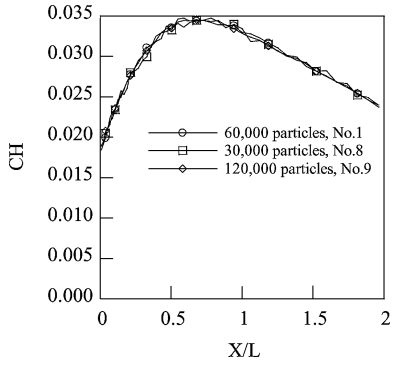

Fig. 15 Effects of the number of particles on heat transfer rate distributions on the plate.

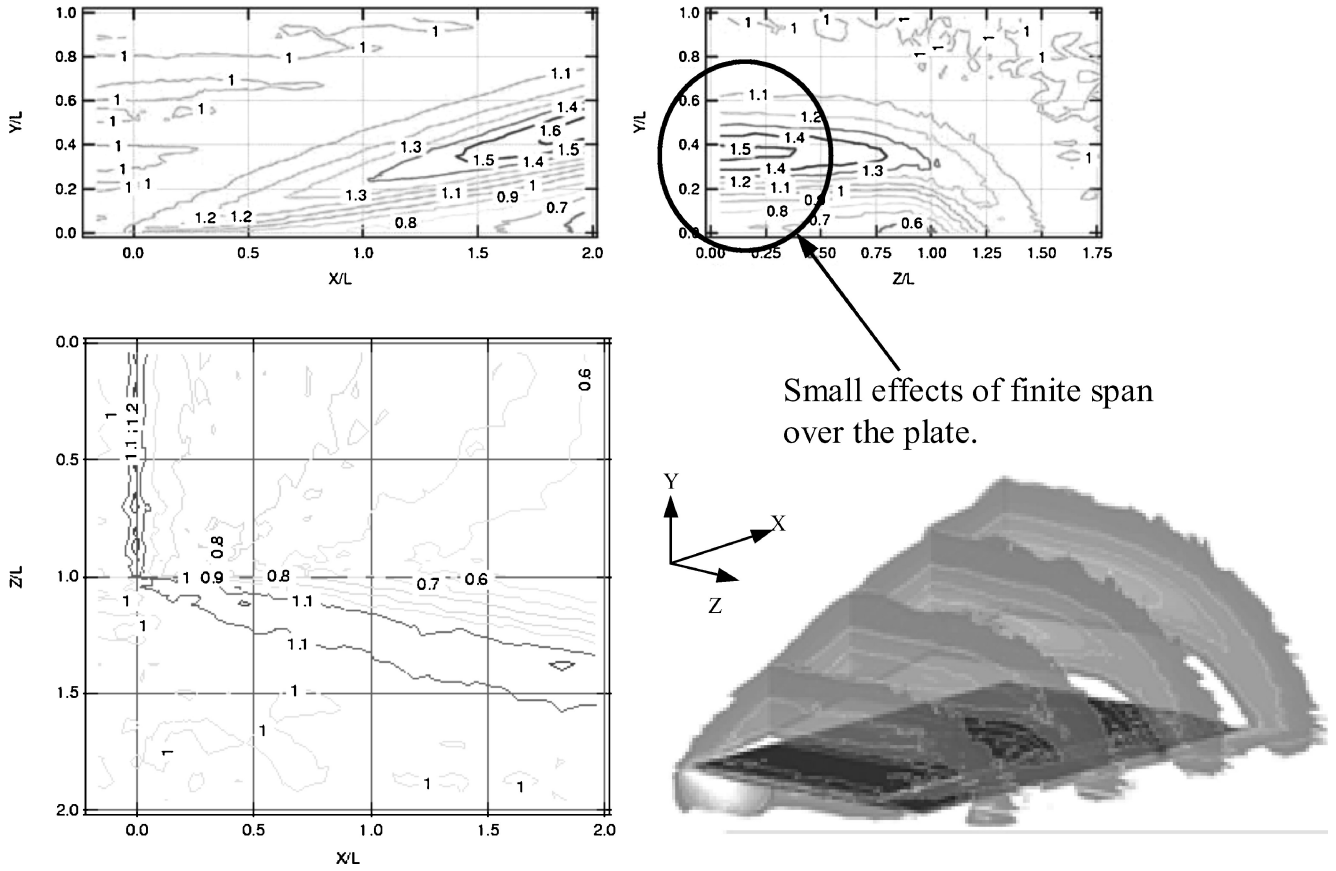

Fig. 16 Density contours over the flat plate (top left: cross section at $Z/L = 0$; top right: cross section at $X/L = 1.5$; bottom left: cross section at $Y/L = 0$; bottom right: density contours at each cross section over the half-width of the plate).

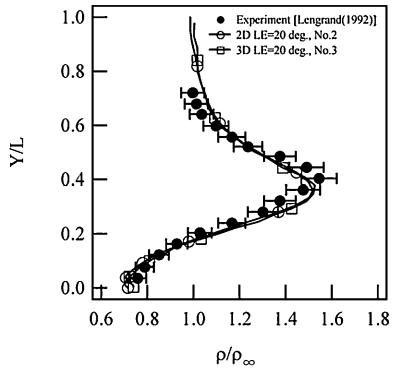

Fig. 17 Comparison between two- and three-dimensional density profiles at $X/L = 1.5$.

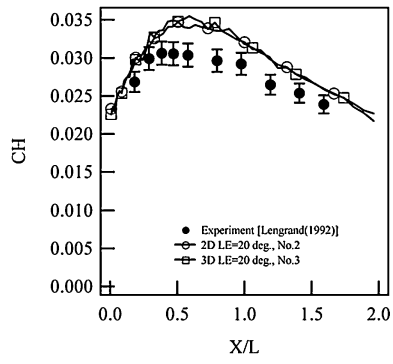

Fig. 18 Comparison between two- and three-dimensional heat transfer rate distributions on the plate.

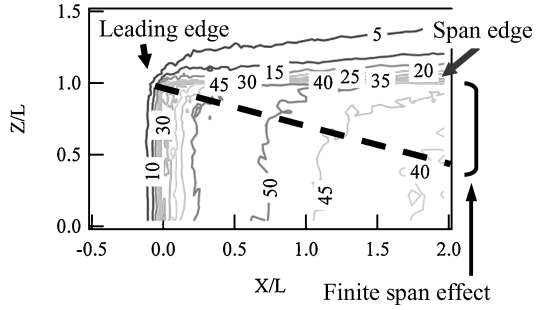

Fig. 19 Normalized translational temperature contours on the plate for the three-dimensional simulation.

the span edge, the difference between translational and rotational temperature increases (Fig. 21) because of the finite span effects. The current results (Figs. 19, 20, and 22) from cells adjacent to the plate identify the domain of influence for the finite plate edge effects. The domain of influence does not reach the plate centerline, but one cannot ignore such effects on plates in hypersonic flows.

The comparisons show that the DSMC results did not coincide with the experimental results. Several possible factors for the discrepancy from the experimental side should be considered: 1) flow nonuniformity at the nozzle exit, 2) rotational temperature freezing in the nozzle, 3) vibrational excitation, and 4) gas–surface interaction. For flow nonuniformity at the nozzle exit, Allègre et al.[13] measured density distributions behind the nozzle exit. The results show that density gradients exist at the nozzle exit due to both a thick nozzle boundary layer and a conical nozzle length. As for the rotational temperature freezing in the nozzle, the influence is believed to be significant; however, the effect was not estimated. The vibrational excitation for $T_0 = 1100$ K should be small because the excitation rate for $T_0 = 1100$ K is about 10%. Furthermore, the degree of vibrational

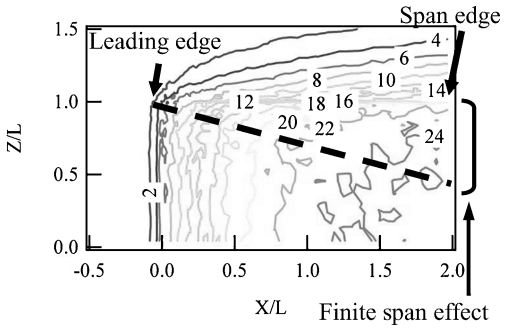

Fig. 20 Normalized rotational temperature contours on the plate for the three-dimensional simulation.

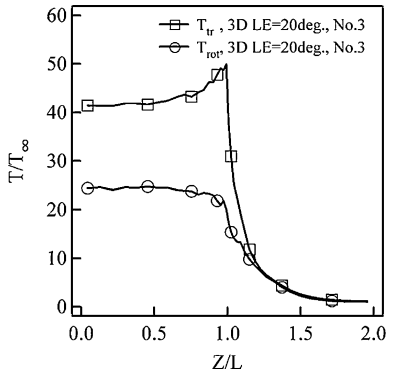

Fig. 21 Translational and rotational temperature distributions on the plate at $X/L = 1.5$.

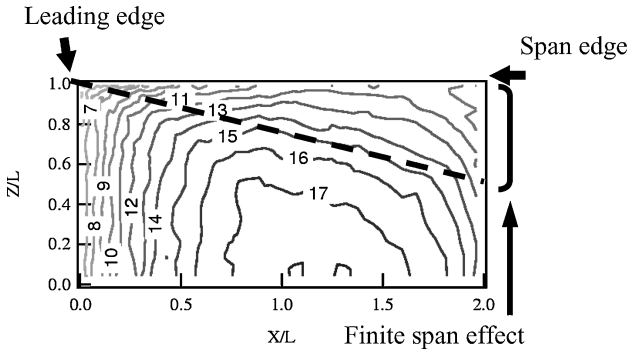

Fig. 22 Pressure distributions on the plate for the three-dimensional simulation.

temperature freezing is larger than that for rotational temperature and is thought to be completely frozen. Finally, the gas–surface interactions are potentially significant in the current flow. The current authors estimated the effects of gas–surface interaction for the same flow conditions with LE = 0 (Ref. 14) and concluded that this issue should be examined. Therefore, the effects of several factors on the experiments should be estimated so that the experimental data can be used for validation of computational simulations.

Microscopic State in the Nonequilibrium Flow

In past research, rotational energy distributions have been estimated by experimental and numerical methods. For example, rotational energy distributions in a normal shock wave were measured using the electron beam fluorescence method by Robben and Talbot.[15] They showed that the rotational energy distributions in the shock wave had non-Maxwell–Boltzmann (MB) distributions for a nitrogen gas in a hypersonic flow with $M_\infty = 7.0$ and 12.9. Both Marrone[16] and Ashkenas[17] presented non-MB rotational energy distributions for a free jet.

Boyd constructed a model for simulating rotational energy relaxation with the DSMC[18] and compared his results with the experimental results measured by Robben and Talbot. Koura proposed a method to combine the MD simulations for molecular collision and the DSMC method for molecular movement.[19] He also showed non-MB rotational energy distributions in a nitrogen normal shock wave. Tokumasu and Matsumoto also presented non-MB rotational energy distributions for a nitrogen normal shock wave.[9] However, they did not discuss translational energy distributions in the shock wave because it is difficult to measure experimental translational energy distributions in detail. In the present section, translational and rotational energy distributions are presented to discuss the detailed structure and transition process of nonequilibrium flow over the flat plate.

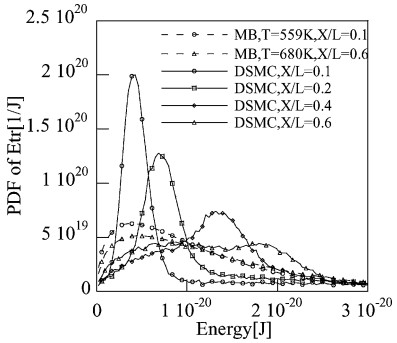

Fig. 23 Translational energy distributions on the plate ($0.1 \le X/L \le 0.6$) for simulation condition 2.

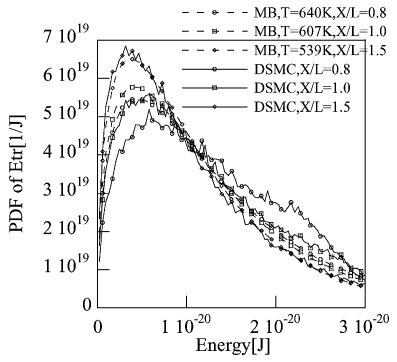

Fig. 24 Translational energy distributions on the plate ($0.8 \le X/L \le 1.5$) for simulation condition 2.

Figures 23 and 24 show translational energy distributions on the plate for simulation condition 2. Some of the MB distributions with $T = T_{tr}$ are also included. Translational temperature at the same location on the plate is plotted in Fig. 11. Figures 23 and 24 show that the PDF of E_{tr} at $X/L = 0.1$ has an extreme peak at low energy and that the peak moves toward larger translational energy as X/L increases. There are two peaks in the PDF distributions at $X/L = 0.6$, where translational temperature begins to decrease, in Fig. 11. These PDF distributions completely differ from a MB distribution. The DSMC translational energy distribution results begin to be similar to MB distributions at $X/L = 1.5$. Figures 25 and 26 show rotational energy distributions on the plate. The distributions are normalized by the lowest sampled rotational energy E_{rot_0}. Rotational temperature at the same location on the plate is also plotted in Fig. 11. Some of the MB distributions with $T = T_{rot}$ are also shown in those figures. The results show that the rotational energy distribution of the DSMC results at $X/L = 0.1$ is completely different from the MB distribution, and its population is large near the lower rotational energy. As the X/L position increases, the rotational energy population of the DSMC results in higher rotational energy increases. At $X/L = 1.5$, it becomes an MB distribution, that is, an equilibrium state.

The energy exchange process between translational and rotational energy, when going from a nonequilibrium state to an equilibrium state in the DSMC, results in a very interesting phenomenon. This nonequilibrium state for a flow over a plate is similar to that in a

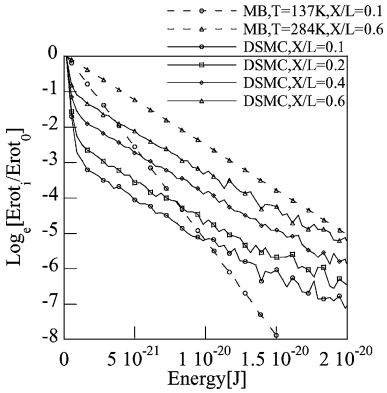

Fig. 25 Rotational energy distributions on the plate ($0.1 \le X/L \le 0.6$) for simulation condition 2.

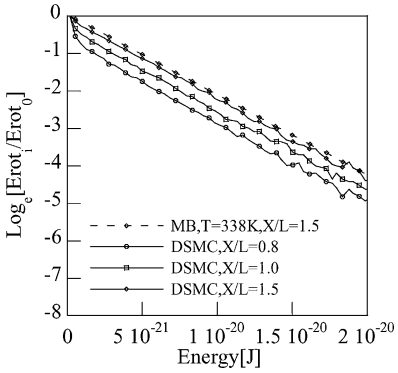

Fig. 26 Rotational energy distributions on the plate ($0.8 \le X/L \le 1.5$) for simulation condition 2.

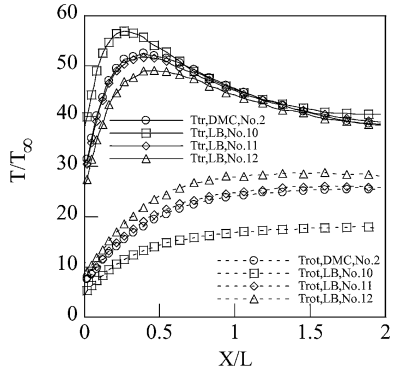

Fig. 27 Comparison of translational and rotational temperature distributions on the plate.

freejet expansion and that in a normal shock wave. The LB model, which has been widely used in DSMC simulations, is based on equilibrium properties and has a parameter to control the ratio of elastic collisions to inelastic collisions. Then a comparison between the DMC model and LB model is carried out. At first, a comparison of translational and rotational temperature distributions is shown in Fig. 27. When the fraction of inelastic collision, ϕ, increases, the maximum peak for translational temperature decreases, whereas rotational temperature increases altogether. From the present results, the LB model is significantly sensitive for ϕ. The results of the DMC model are similar to those of the LB with $\phi = 0.5$ (simulation condition 11).

Figures 28 and 29 show a comparison of translational energy distributions on the plate at $X/L = 0.5$ and 1.5. The translational energy distributions for the LB model (condition 10) become an equilibrium state faster than the other cases. The results for the DMC model (condition 2) are similar to those for the LB model with $\phi = 0.5$

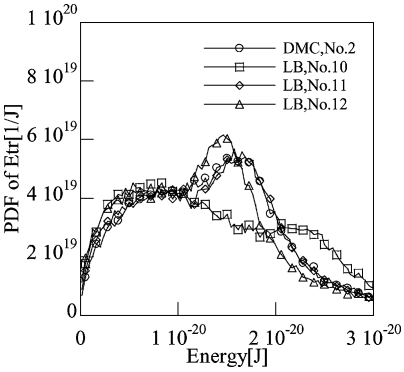

Fig. 28 Comparison of translational energy distributions on the plate at $X/L = 0.5$.

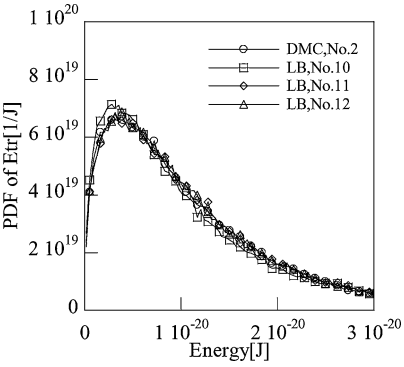

Fig. 29 Comparison of translational energy distributions on the plate at $X/L = 1.5$.

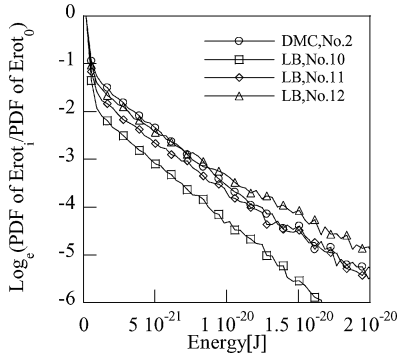

Fig. 30 Comparison of rotational energy distributions on the plate at $X/L = 0.5$.

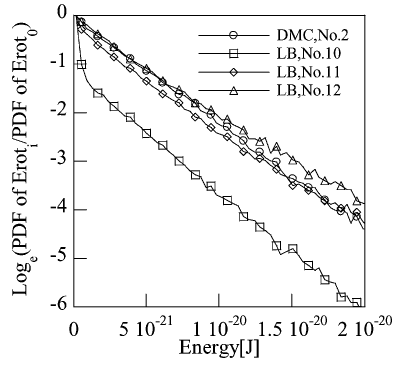

Fig. 31 Comparison of rotational energy distributions on the plate at $X/L = 1.5$.

(condition 11). Rotational energy distributions in Figs. 30 and 31 show that the LB model shows non-MB distributions; however, these distributions are strongly dependent on the parameter ϕ. The results for the LB model (condition 12) still remain non-MB distributions at $X/L = 1.5$. The results of the DMC model distributed between the LB model with $\phi = 0.5$ (condition 11) and $\phi = 1.0$ (condition 12).

The LB model cannot simulate nonequilibrium flow accurately and produces different distributions that may depend on the parameter selected. The present simulations, which were constructed based on the MD simulation, were shown to have the ability to simulate the transition in detail by using the DMC model without resorting to assumed parameters.

Conclusions

Two- and three-dimensional DSMC simulations based on multiscale analysis were conducted for nonequilibrium rarefied gas flow around a flat plate with a sharp leading edge. The results of two-dimensional simulations show that the leading edge affects the flow over the plate due to a shock wave generated by the beveled leading edge. The pressure and heat transfer rate on the plate increase in the vicinity of the leading edge due to the leading edge effects; however, there exists a discrepancy between DSMC results and experimental results.

Sensitivity analyses for two-dimensional simulations were carried out. The results showed that the temperature distributions on the plate were affected by the number of computational cells; however, there was no influence with regard to time step and the number of particles.

Results of three-dimensional simulations show finite span effects that are very pronounced. However, differences between the two- and three-dimensional results do not appear in the symmetry plane of the plate because the plate is sufficiently short to avoid the finite span effects.

Microscopic states in the nonequilibrium flow for the two-dimensional simulation show that non-Maxwell–Boltzmann distribution in the translational and rotational energy distributions occur. This nonequilibrium state for the flow over the plate is similar to that for a freejet expansion. The rapid excitation for lower translational energy appears; then rotational energy excites from a lower energy level because of the transition between translational and rotational energy. Finally, the comparison between the LB model and the DMC model showed that the DMC model could simulate the transition in detail without having to resort to assumed parameters.

Acknowledgments

N. Tsuboi and H. Yamaguchi are supported by research fellowships from the Japan Society for the Promotion of Science for Young Scientists. We thank J. C. Lengrand, Centre National de la Recherche Scientifique, for providing his experimental condition and experimental accuracy.

References

[1]Stolley, J. L., "Viscous Interaction Effects on Re-Entry Aerothermodynamics: Theory and Experimental Results, in Aerodynamics Problems of Hypersonic Vehicles," *AGARD Lecture Series*, Vol. 1, No. 42, 1972, pp. 10-1–10-28.

[2]Bird, G. A., *Molecular Gas Dynamics*, Clarendon, Oxford, 1976.

[3]Nanbu, K., "Direct Simulation Scheme Derived from the Boltzmann Equation. I. Monocomponent Gases," *Journal of the Physical Society of Japan*, Vol. 49, 1980, pp. 2042–2049.

[4]Lengrand, J., Allègre, J., Chpoun, A., and Raffin, M., "Rarefied Hypersonic Flow over a Flat Plate: Numerical and Experimental Results," *Proceedings of the 18th International Symposium on Rarefied Gas Dynamics*, edited by B. D. Shizgal and D. P. Weaver, Vol. 160, AIAA, Washington, DC, 1992, pp. 276–284.

[5]Allègre, J., Raffin, M., Chpoun, A., and Gottesdiener, L., "Rarefied Hypersonic Flow over a Flat Plate with Truncated Leading Edge," *Proceedings of the 18th International Symposium on Rarefied Gas Dynamics*, edited by B. D. Shizgal and D. P. Weaver, Vol. 160, AIAA, Washington, DC, 1992, pp. 285–295.

[6]Chpoun, A., Lengrand, J. C., and Heffner, K. S., "Numerical and Experimental Investigation of Rarefied Compression Corner Flow," AIAA Paper 92-2900, July 1992.

[7]Heffner, K. S., Gottesdiener, L., Chpoun, A., and Lengrand, J. C., "Leading Edge Effect on Rarefied Hypersonic Flow over a Flat Plate," AIAA Paper 91-1749, June 1991.

[8]Borgnakke, C., and Larsen, P. S., "Statistical Collision Model for Monte Carlo Simulation of Polyatomic Gas Mixture," *Journal of Computational Physics*, Vol. 18, No. 4, 1975, pp. 405–420.

[9]Tokumasu, T., and Matsumoto, Y., "Dynamic Molecular Collision (DMC) Model for Rarefied Gas Flow Simulations by the DSMC Method," *Physics of Fluids*, Vol. 11, No. 7, 1999, pp. 1907–1920.

[10]Koura, K., "Null-Collision Technique in the Direct-Simulation Monte Carlo Method," *Physics of Fluids*, Vol. 29, No. 3, 1986, pp. 3509–3511.

[11]Dietrich, S., and Boyd, I. D., "Parallel Implementation on the IBM SP-2 of the Direct Simulation Monte Carlo Method," AIAA Paper 95-2029, June 1995.

[12]Wilmoth, R. G., "Application of a Parallel Direct Simulation Monte Carlo Method to Hypersonic Rarefied Flows," *AIAA Journal*, Vol. 30, No. 10, 1992, pp. 2447–2452.

[13]Allègre, J., Bisch, D., and Lengrand, J., "Experimental Rarefied Density Flowfields at Hypersonic Conditions over 70-Degree Blunted Cone," *Journal of Spacecraft and Rockets*, Vol. 34, No. 6, 1997, pp. 714–718.

[14]Tsuboi, N., and Matsumoto, Y., "Numerical Simulation of Interaction Between Shock Waves and Boundary Layer in Nonequilibrium Hypersonic Rarefied Flow," *Proceedings of the 22nd International Symposium on Shock Waves*, edited by G. J. Ball, R. Hillier, and G. T. Roberts, Vol. 2, Imperial College, London, 1999, pp. 909–914.

[15]Robben, F., and Talbot, L., "Experimental Study of the Rotational Distribution Function of Nitrogen in a Shock Wave," *Physics of Fluids*, Vol. 9, No. 4, 1966, pp. 653–662.

[16]Marrone, P. V., "Temperature and Density Measurement in Free Jets and Shock Waves," *Physics of Fluids*, Vol. 10, No. 3, 1967, pp. 521–538.

[17]Ashkenas, H., "Rotational Temperature Measurements in Electron-Beam Excited Nitrogen," *Physics of Fluids*, Vol. 10, No. 12, 1967, pp. 2509–2520.

[18]Boyd, I. D., "Relaxation of Discrete Rotational Energy Distributions Using a Monte Carlo Method," *Physics of Fluids A*, Vol. 5, No. 9, 1993, pp. 2278–2286.

[19]Koura, K., "Monte Carlo Direct Simulation of Rotational Relaxation of Diatomic Molecules Using Classical Trajectory Calculations: Nitrogen Shock Wave," *Physics of Fluids*, Vol. 9, No. 11, 1997, pp. 3543–3549.

J. C. Taylor
Associate Editor